



Spectral solution of the inverse Mie problem



Andrey V. Romanov^{a,b}, Anastasiya I. Konokhova^a, Ekaterina S. Yastrebova^{a,b},
Konstantin V. Gilev^{a,b}, Dmitry I. Strokotov^{a,c}, Andrei V. Chernyshev^{a,b}, Valeri P. Maltsev^{a,b,c},
Maxim A. Yurkin^{a,b,*}

^a Voevodsky Institute of Chemical Kinetics and Combustion SB RAS, Institutskaya Str. 3, 630090, Novosibirsk, Russia

^b Novosibirsk State University, Pirogova Str. 2, 630090, Novosibirsk, Russia

^c Novosibirsk State Medical University, Krasny Prospect 52, 630091, Novosibirsk, Russia

ARTICLE INFO

Article history:

Received 17 February 2017

Revised 28 April 2017

Accepted 28 April 2017

Available online 29 April 2017

Keywords:

Light scattering

Inverse problem

Mie theory

Fourier spectrum

Single-particle characterization

ABSTRACT

We developed a fast method to determine size and refractive index of homogeneous spheres from the power Fourier spectrum of their light-scattering patterns (LSPs), measured with the scanning flow cytometer. Specifically, we used two spectral parameters: the location of the non-zero peak and zero-frequency amplitude, and numerically inverted the map from the space of particle characteristics (size and refractive index) to the space of spectral parameters. The latter parameters can be reliably resolved only for particle size parameter greater than 11, and the inversion is unique only in the limited range of refractive index with upper limit between 1.1 and 1.25 (relative to the medium) depending on the size parameter and particular definition of uniqueness. The developed method was tested on two experimental samples, milk fat globules and spherized red blood cells, and resulted in accuracy not worse than the reference method based on the least-square fit of the LSP with the Mie theory. Moreover, for particles with significant deviation from the spherical shape the spectral method was much closer to the Mie-fit result than the estimated uncertainty of the latter. The spectral method also showed adequate results for synthetic LSPs of spheroids with aspect ratios up to 1.4. Overall, we present a general framework, which can be used to construct an inverse algorithm for any other experimental signals.

© 2017 Elsevier Ltd. All rights reserved.

1. Introduction

Light scattering is ubiquitous in nature and technology and is often the only or the most feasible approach to characterize particles or particle systems [1]. Many characterization techniques address the particle ensemble as a whole, due either to a large scattering volume [2,3] or to the dense packing of individual components [4]. However, they are inherently ill-posed in trying to retrieve the distribution of the ensemble over the particle characteristics [2,5]. Single-particle techniques show greater promise in detailed and robust characterization, at least in the controlled laboratory conditions [6,7].

Successful single-particle characterization requires three ingredients: measurement, simulation, and inversion. The typical measured signals consist of a few scalar values [8,9], an angle-resolved light-scattering pattern (LSP), [10,11] or a two-dimensional LSP [12,13]. The simulation part benefits from several well-established methods and open-source codes [4,14]. It is now easy to simulate

light scattering by almost any complex inhomogeneous particle, while the main complexity comes from the vastness of the multidimensional space of possible particle characteristics [15,16]. The ultimate solution for the inverse problem would be a direct imaging (tomography) approach with no prior assumptions about the object. However, all existing attempts employ 2D LSPs for many orientations of the same particle and either assume weak scattering (Rayleigh-Debye-Gans approximation) [17,18] or require phase of the scattered field to be measured as well [19,20]. Otherwise, one has to assume a particle shape model a priori, reducing the problem to determining several characteristics of this model. Such characterization methods can be tentatively divided into 3 broad categories: nonlinear regression, machine learning, and parametric (compression) techniques.

Nonlinear regression is based on the direct comparison of experimental signals (typically, LSPs) with simulated ones, using some norm of the difference (residual). Global minimization of this residual is a challenging task with computational complexity rapidly increasing with the number of shape characteristics [15,21]. This complexity can be partly concentrated into a one-time investment of computational power using precalculated (look-up) database of LSPs [22–24]. This makes it possible to apply

* Corresponding author.

E-mail address: yurkin@gmail.com (M.A. Yurkin).

nonlinear regression routinely for particles without spherical symmetry, such as red blood cells [25], platelets [26], and rod-shaped bacteria [27]. Moreover, in addition to the best-fit particle characteristics one can construct confidence intervals for these characteristics, i.e. evaluate the characterization errors [23,26,28].

Machine learning is an extremely broad class of methods, but we discuss only neural networks as the most representative example. Ideally, this approach should be able to automatically train itself on a large set (database) of LSPs with known characteristics and handle high-dimensional problems [29]. But, practically, its performance is hard to predict and it may require a lot of fine tuning. So far the neural networks has only been used for light-scattering characterization of spherical particles [30,31] and red blood cells [32], as recently reviewed in [33]. Moreover, those methods do not use the whole LSP, but only a number of parameters derived from it.

This compression of an experimental signal into several (two-three) parameters is central to the third class of characterization methods. The parameters are extracted either directly from the measured signal, e.g. the LSP [34,35] or the time-resolved signal [36], or from its Fourier [37,38] or Gegenbauer [39] spectrum. Alternatively the amount of experimental data may originally be limited to only a couple of numbers [8,9]. The specific way to process the signal parameters can vary a lot, but all parametric methods have very high speed in determining a small number of particle characteristics (typically, only the size and, sometimes, the refractive index). They are also potentially more stable to instrumental noise and distortions, as well as to distortions of the optical model. The most popular parametric method is the spectral sizing [40–42], which is based on almost linear relation between the size of a sphere and characteristic frequency of its LSP or, equivalently, the position of the main peak in the Fourier spectrum of the LSP. Interestingly, the spectral sizing of homogeneous spheres [43] can be extended with virtually no changes to estimation of diameters of leukocytes [44] and red blood cells [45], although the accuracy of this estimation has not been thoroughly tested. Moreover, estimation of sphere refractive index has been proposed (without assessing the accuracy) in a limited range of size and refractive index, using the integral of the LSP as a second parameter [46].

Each of the three above classes has its pros and cons, and occupies a certain application niche. This paper is devoted to the systematic development of the spectral method with the goal to fully characterize a homogeneous sphere, i.e. to solve the inverse Mie problem both quickly and robustly. For that we compress the whole measured LSP into two parameters of its power Fourier spectrum, which are further transformed into two characteristics of the particle. In Section 2 (and Appendix A) we construct this characterization method starting with a LSP measured with the scanning flow cytometer (SFC) [11,43]. However, the provided details should enable one to repeat the whole procedure for any other experimental set-up and/or signal parameters. We also perform a detailed theoretical analysis of the underlying map and applicability (uniqueness) domain of the developed method. In Section 3 we describe two sets of experimental measurements, namely milk fat globules and spherized red blood cells, and a set of synthetic data for spheroids. Those data, affected by both instrumental noise and optical-model distortions, are used for thorough testing of the characterization method in Section 4. We conclude the paper in Section 5.

2. Spectral characterization method

In this Section we construct a method to determine both diameter d and refractive index n of a spherical particle from the spectrum of its LSP. The main idea is to compress the whole LSP spectrum into two parameters, to describe the direct problem as a

map of particle characteristics into those parameters ($G: \mathbb{R}^2 \rightarrow \mathbb{R}^2$), and to invert this map by constructing an interpolant. To abstract from specific wavelength of the incident light λ and medium refractive index n_0 we further describe the particle by its size parameter $x = \pi d n_0 / \lambda$ (d – sphere diameter) and relative refractive index $m = n/n_0$. We also limit ourselves to non-absorbing particles, i.e. assume real m . Moreover, we consider only $m > 1$, while the case of $0 < m < 1$ is expected to be qualitatively similar. Allowing m to take values on both sides of unity will, most probably, break the uniqueness of the inverse problem in the whole range of particle characteristics.

2.1. Power spectrum and its parameters

Let us define the specific form of a LSP spectrum. We start with the standard LSP, measured by the SFC:

$$I(\theta) = \int_0^{2\pi} d\varphi [S_{11}(\theta, \varphi) + S_{14}(\theta, \varphi)], \quad (1)$$

where S is the Mueller scattering matrix [47], θ and φ are the polar and azimuthal scattering angles, and $S_{14} \equiv 0$ for ideal spheres. To keep the discussion manageable we further only consider the LSP in the range from $\theta_1 = 10^\circ$ to $\theta_2 = 65^\circ$ and apply the same spectral transformation as in [43]. Specifically, the LSP is multiplied by the Hanning window function

$$w(\theta) = \sin^2\left(\pi \frac{\theta - \theta_1}{\theta_2 - \theta_1}\right), \quad (2)$$

and its power Fourier spectrum on this finite range is computed:

$$P(q) = \left| \frac{1}{\theta_2 - \theta_1} \int_{\theta_1}^{\theta_2} d\theta w(\theta) I(\theta) \exp(-2\pi i q \theta) \right|^2, \quad (3)$$

which is normalized to be only weakly dependent on a particular choice of the angular range. The practical calculations are performed with the fast Fourier transform using uniform discretization over $N = 256$ intervals with further zero-padding up to $M = 4096$ points (to increase the spectral resolution):

$$P(q_k) = \left| \frac{1}{N} \sum_{j=0}^{N-1} w(\theta_1 + j\Delta\theta) I(\theta_1 + j\Delta\theta) \exp\left(-i \frac{2\pi}{M} k j\right) \right|^2, \quad (4)$$

where $\Delta\theta = (\theta_2 - \theta_1)/N$ and $q_k = k/(M\Delta\theta)$. This procedure is illustrated in Fig. 1, where we also defined the spectral parameters: location (L) and amplitude (A_p) of non-zero spectral peak and amplitude of zero frequency (A_0). L can also be called the main (angular) frequency, while A_0 is the squared average value of the windowed LSP – similar to the parameter used in [46]. The peak parameters are determined by the quadratic fit with a window width of 15 points (0.98 rad^{-1}). While we conventionally use units of degree for θ , we employ the dimensional SI units (rad^{-1}) for q and L and omit it further. Note also, that the Mueller matrix S and, hence, I and P are dimensionless. However, their scales (used in all figures) are unambiguously defined by Eqs. (1)–(4). In other words, arbitrary units are not used anywhere.

Almost linear relation between x and L , with x/L roughly equal to π , is well-known [43,48] and can be understood using simple arguments of diffraction gratings or the Rayleigh-Debye-Gans (RDG) approximation [47]. The choice of the second parameter (to deduce m as well) is less obvious. Relative peak amplitude A_p/A_0 has been briefly discussed previously [43,45]; here we also consider both A_0 and A_p separately. However, as shown in Section 4.1, A_0 is the most robust (insensitive) with respect to experimental distortions of the LSP. Therefore, we base the production algorithm on this parameter and use it as a primary example in the following discussion. The corresponding analysis for other two parameters is

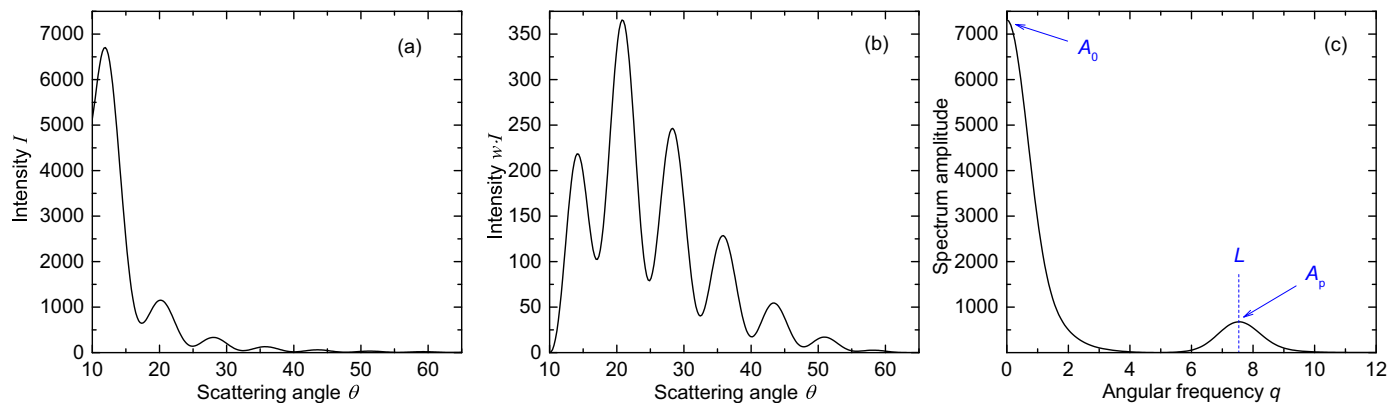


Fig. 1. Original (a) and windowed (b) LSPs and its power spectrum (c) for a sphere with $x=24$ and $m=1.083$.

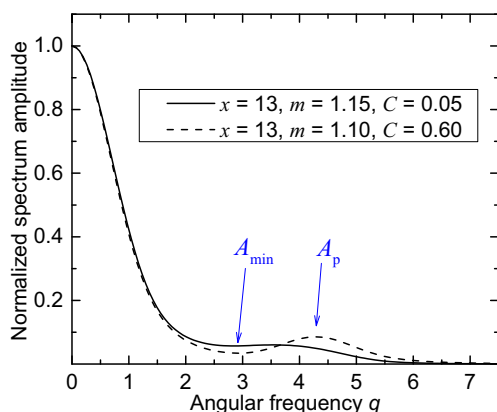


Fig. 2. Normalized (to zero frequency) power spectrum for $x=13$ spheres with $m=1.15$ and 1.10 . Values of the contrast C are shown in the legend.

presented in Appendix A. While using additional spectral parameters can definitely improve the performance of the algorithm, we explicitly limit ourselves to using a single amplitude (i.e. in total two spectral parameters). Apart from the simplicity of the final algorithm, this allows us to visualize and analyze in detail the underlying map G and to gain confidence in the solution in contrast to, e.g., neural-net-type methods.

We must stress that the spectral peak is not always present. There are cases where it overlaps with a zero-frequency bump (Fig. 2). To quantify this problem we introduce the Weber contrast:

$$C = 1 - \frac{A_{\min}}{A_p}, \quad (5)$$

where A_{\min} is the minimum value to the left of the main peak ($C=0$ if there is no minimum at all). The closer C comes to zero, the greater the error becomes, especially in determining L from real experimental data. The dependence of C on x and m is shown in Fig. 3, based on which we further limit ourselves to the range $x \in [11, 100]$ and $m \in [1, 1.5]$. The upper limit of x is rather arbitrary and can be extended if needed, see Fig. 7(a).

2.2. Inverse problem and uniqueness of solution

We construct a dense uniform grid (200×200) in the above-mentioned range of x and m and calculate a LSP and spectral parameters for each grid point. 62 nodes of this grid fall into the

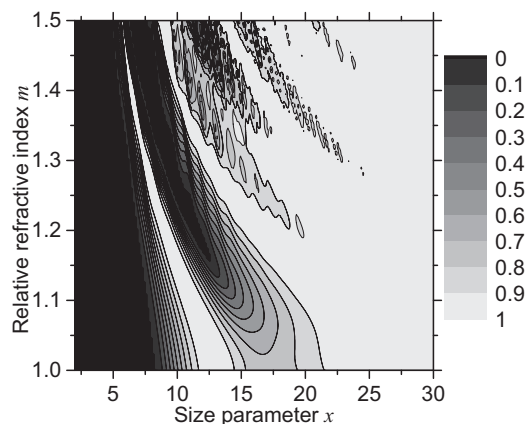


Fig. 3. Contour plot of the spectrum contrast C for spheres versus x and m .

black region in Fig. 3 and are omitted from further analysis. The resulting values of L and A_0 are shown in Fig. 4, while corresponding results for A_p and A_p/A_0 – in Fig. A1. However, we can consider those results more generally – as a dense cloud in a four-dimensional space (x, m, L, A_0) . Then Fig. 4 depicts two 3D projections of this space, while another two projections, (L, A_0, x) and (L, A_0, m) (Fig. 5), seemingly solve the inverse Mie problem. Corresponding projections for other amplitudes (A_p and A_p/A_0) are shown in Fig. A2.

The major remaining problem is that Fig. 5 does not define a single-valued function over the whole domain of (L, A_0) . In particular, the larger- A_0 side of both x and m surfaces contain multiple branches and large derivatives, resulting in fragmentation into seemingly isolated dots. This problem is especially pronounced for m , making its determination impossible in this region. To gain more understanding of this issue let us take a more detailed look at Fig. 4(b). Slicing it at constant size ($x=24$) we obtain a typical dependence of A_0 on m (Fig. 6), featuring monotonous increase for smaller m , but complex oscillation for $m > 1.2$. The latter oscillations also significantly depend on a particular value of x , as typical for the Mie theory.

Naturally one can only hope to invert the map G in a limited domain of uniqueness, but defining this domain is not trivial. Let us first discuss it using 1D case of Fig. 6 as an example. The first option is a domain of m , in which $A_0(m)$ is a monotonous function – from the origin to the first maximum, see Fig. 6(a).

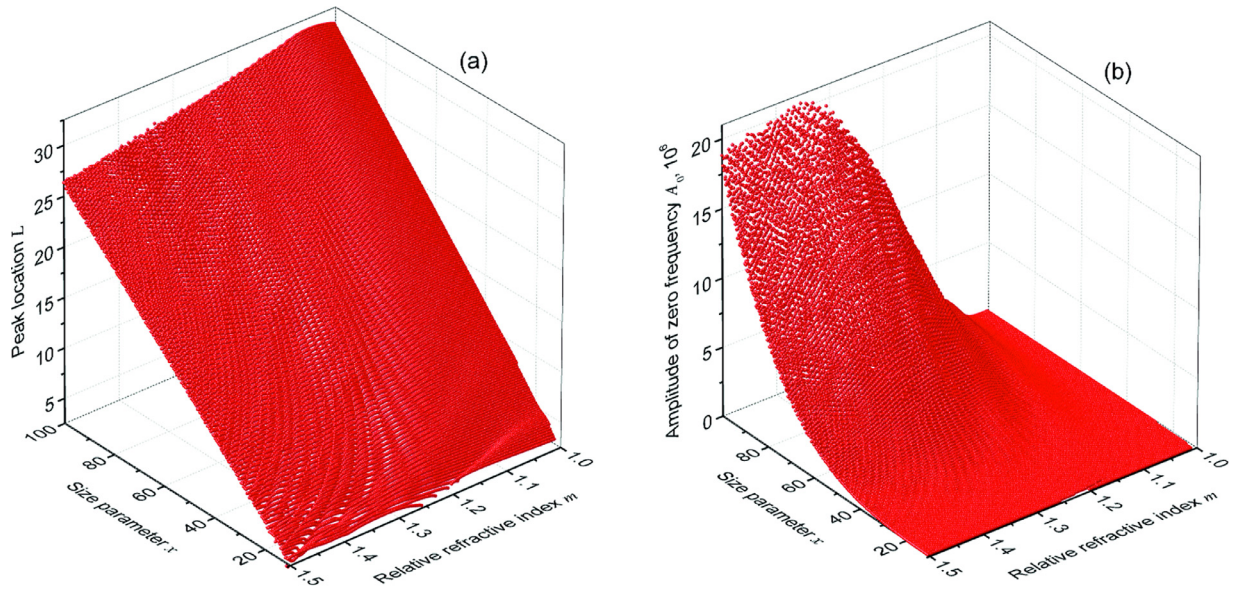


Fig. 4. The dependence of L (a) and A_0 (b) for spheres on x and m .

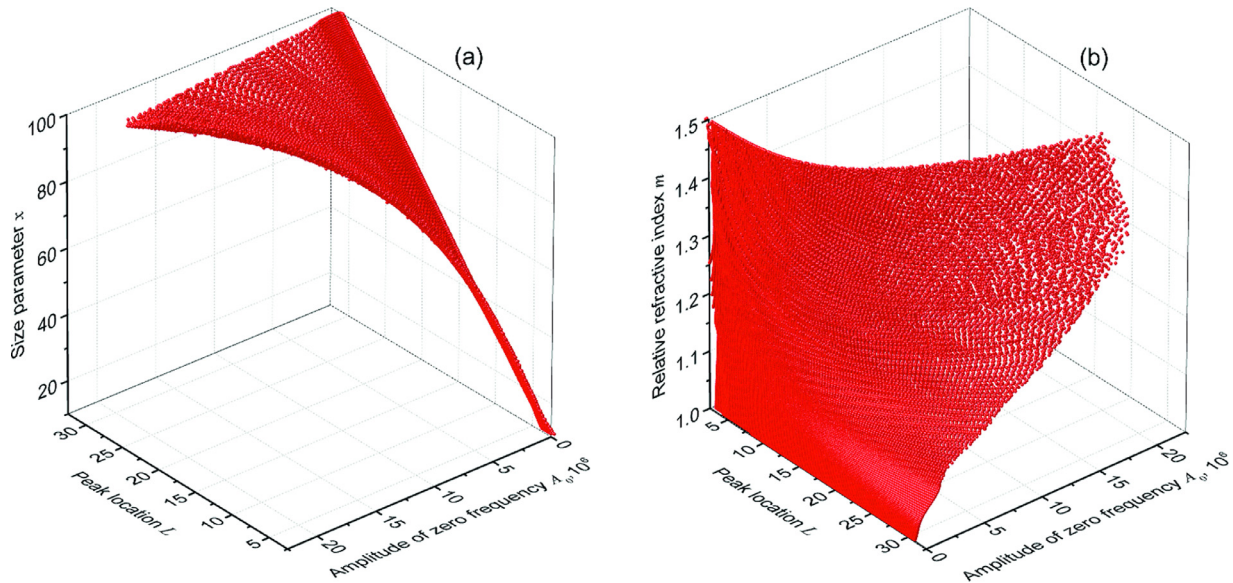


Fig. 5. Scatter plot of x (a) and m (b) versus L and A_0 , based on the same theoretical data as Fig. 4. Axes directions differ between the figure parts for clarity.

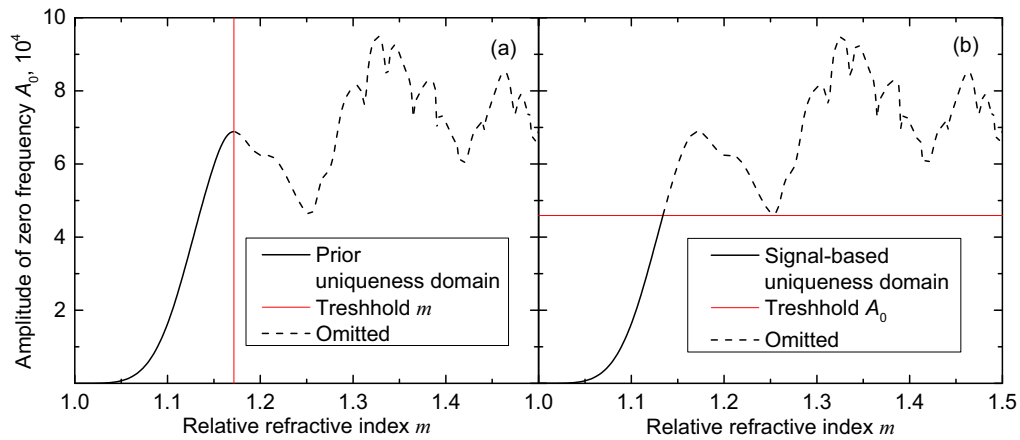


Fig. 6. Dependence of A_0 on m for $x=24$ and illustration of two strategies to define uniqueness domains: a priori (argument-based) (a) and signal-based (b). straight red lines denote the threshold values, dashed and solid black curves – omitted and remaining parts of the function graph to be inverted. (For interpretation of the references to color in this figure legend, the reader is referred to the web version of this article.)

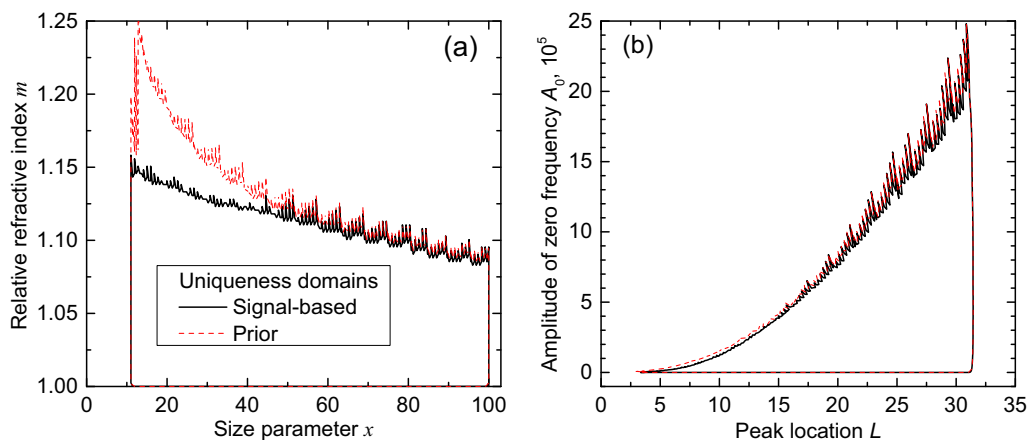


Fig. 7. Prior and signal-based uniqueness domains in terms of x and m (a), L and A_0 (b). left, right, and bottom boundaries for signal-based uniqueness domains coincide with that for corresponding prior ones.

This corresponds to a standard branch of a multi-valued inverse function (e.g., in complex analysis) and we further denote it as a *prior* uniqueness domain. Inconveniently, it is based on assumption about values of m , which is hard to verify for real particles in some applications. An alternative option is to define a *signal-based* uniqueness domain using only the function values (experimental signals). Fortunately, as shown in Fig. 6(b), there exists a threshold such that for smaller A_0 the inverse problem is guaranteed to have a unique solution. There is, however, a trend of decreasing A_0 down to zero for larger m (data not shown, but see Fig. 8), which makes it impractical to build signal-based uniqueness domain using the whole set of $m > 1$. Thus, we still need to employ prior assumption about m , but it can be varied to fit any specific application in contrast to the prior uniqueness domain. In particular, here and further we implicitly limit m to the range [1,1.5] as specified earlier. Analogous plots for $A_p(m)$ and $A_p/A_0(m)$ are shown in Fig. A3.

If one rotates Fig. 6 by 90° and considers it as a plot of inverse function $m(A_0)$, the definition of the uniqueness domains could be restated as regions from the origin to the infinite derivative of the main branch $m(A_0)$ and to the first occurrence of multiple values, respectively. In this form those definitions can be directly generalized to the two-dimensional map G , replacing $m(A_0)$ by $x(L, A_0)$ and $m(L, A_0)$. However, rigorous calculation of such uniqueness domains is arduous; hence, we employ an approximate shortcut, assuming that x and L are linearly related. Then we need to consider only $m(L, A_0)$ – its infinite derivatives correspond to that of $m(A_0)$ for a specific x [Fig. 6(a)] and its multiple values appear if and only if $A_0(m)$ is outside of the signal-based uniqueness domain [Fig. 6(b)]. Therefore, the whole uniqueness domain (of each type) in coordinates (x, m) can be obtained by combining corresponding ranges of m , obtained for each x separately. As further results show, e.g., Fig. 9, this approximate method does not introduce any artefacts.

The resulting uniqueness domains are shown in Fig. 7(a), featuring characteristic Mie oscillations. The boundaries of x are determined by the original choice of the grid. However, the lower boundary cannot be significantly lowered due to low contrast of spectral peak (Fig. 3); note also the dip in the prior uniqueness domain for $x \approx 12$. By contrast, the upper boundary of x can be extended, minding the moderate decrease of maximum operational value of m and required fine angular resolution of the measured LSPs. The uniqueness domain can also be presented in terms of L and A_0 [Fig. 7(b)], which facilitates better understanding of differences between the two domains. The prior uniqueness domain is initially defined in terms of x and m , and corresponding particles

are guaranteed to fall within the prior (L, A_0) domain, but not vice versa. In other words, the latter domain plays a secondary role, and can only be used for additional consistency check. By contrast, the signal-based domain is originally defined in terms of L and A_0 , but has one-to-one correspondence with the (x, m) domain. So any particle with the signal inside the (L, A_0) domain can be uniquely characterized, and any particle with characteristics inside the (x, m) domain is guaranteed to have suitable values of L and A_0 . Analogous results for other amplitudes are shown in Fig. A4.

An unexpected feature of Fig. 7 is large similarity of two uniqueness domains for larger x . That is related to the behavior of $A_0(m)$ for such x , a specific example of which (for $x=90$) is shown in Fig. 8. First, it illustrates the abovementioned decreasing trend with increasing m . Second, the general increasing trend in a wide range of m (up to 1.5) is interrupted by almost flat “shoulder” around $m=1.1$. Following our definition, this shoulder containing minor oscillations determines the upper m -boundary of both uniqueness domains. However, ignoring the shoulder will extend the upper boundary of m to a value from 1.2 to 1.4 (see Fig. 8) and will introduce only relatively small errors, comparable to experimental uncertainties in determination of L and A_0 . But we leave this option for future research.

2.3. Interpolation of the inverse map

Given the point-wise representation of the inverse map (Fig. 5), limited to the uniqueness domain (Fig. 7), the only remaining step is to make it operational (easy to compute) for any input pair (L, A_0) . For that we employ interpolation, carried out in two steps. First, we apply triangular linear interpolation to project the original irregular set of points onto the regular grid. Second, we construct bilinear interpolant based on the latter grid.

Additionally, to reduce interpolation errors we preliminary straighten the surfaces of $x(L, A_0)$ and $m(L, A_0)$ as described in the following. By its definition [Eq. (4)] A_0 is the squared average value of the windowed LSP. In the framework of the Rayleigh-Gans-Debye approximation [47] this average value is proportional to $x^2(m-1)^2$, implying

$$A_0 \sim x^4 (m-1)^4 \Rightarrow x (m-1) \sim \sqrt[4]{A_0}. \quad (6)$$

Combining it with approximately linear relation between x and L , we define the *linearized* zero-frequency amplitude as

$$B_0 = \sqrt[4]{A_0}/L \quad (7)$$

with the goal for $m-1$ to be approximately proportional to B_0 . Therefore, we use B_0 instead of A_0 for further processing. In par-

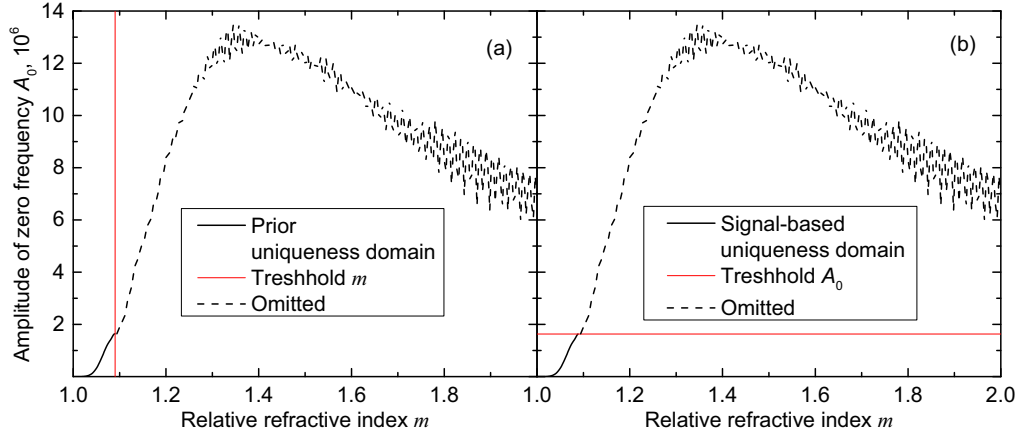


Fig. 8. Same as Fig. 6, but for $x=90$ and in the extended range of m . Red lines, denoting the thresholds for uniqueness domains, are determined by the same small shoulder of the function graph to be inverted. (For interpretation of the references to color in this figure legend, the reader is referred to the web version of this article.)

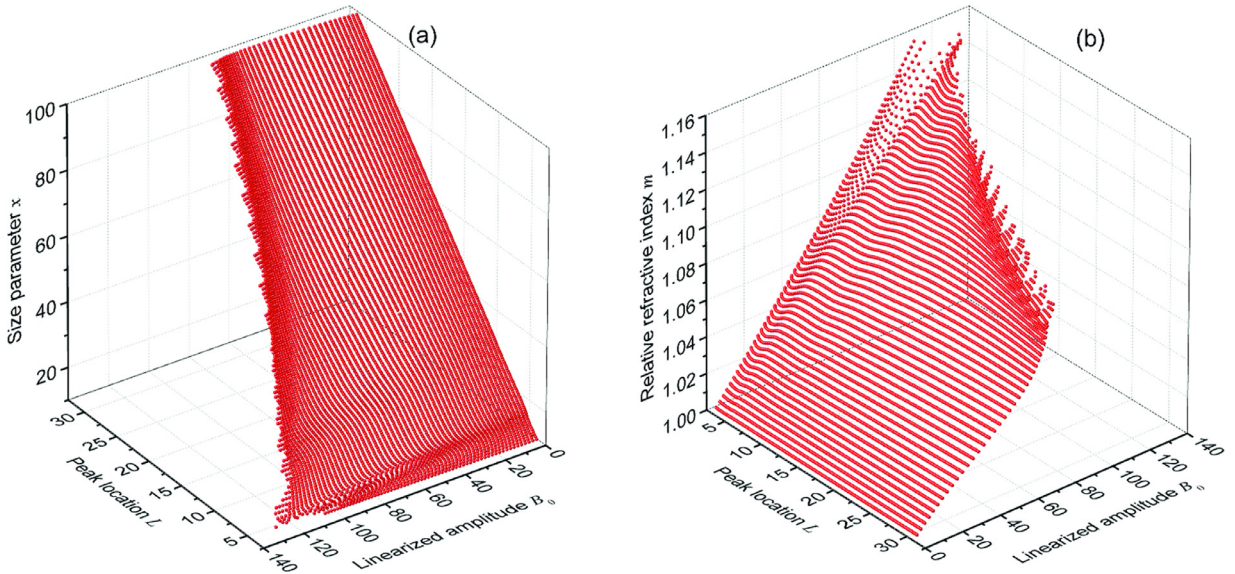


Fig. 9. Same as Fig. 5, but using the linearized amplitude B_0 instead of A_0 and limited to the signal-based uniqueness domain.

ticular, the scatter plots of $x(L, B_0)$ and $m(L, B_0)$ are shown in Fig. 9.

Note that the inherent approximations in the above analysis introduce no errors, since in the end the interpolation does account for any deviations, given sufficiently dense grid. This interpolation together with the intermediate regular grid is shown in Fig. 10. The procedure for other amplitudes is completely analogous, using the following linearization:

$$B_p = \sqrt[4]{A_p/L}, \quad B_p/B_0 = \sqrt[4]{A_p/A_0}. \quad (8)$$

The corresponding interpolants are depicted in Fig. A5.

Finally, one can see that functions $x(L, B_0)$ and $m(L, B_0)$ are almost linear in the shown domain, suggesting a simple approximate expression. Indeed, the following regression relations can be deduced from our data:

$$x \approx 3.20 L, \quad (9)$$

$$m \approx 1 + 0.066 B_0 \approx 1 + 0.135 B_p. \quad (10)$$

They are constructed inside the signal-based uniqueness domains, and only the main influential spectral parameter is left for each particle characteristic, since the dependence on the second parameter is minor but strongly non-linear. Overall, Eqs. (9) and (10) can be considered as extension of the simplest spectral sizing method [43]. However, the detailed analysis (including errors) of these approximations lies beyond the scope of this paper, since our main goal is the rigorous inversion of the underlying 2D map.

To conclude this section, we note that the particular constructed characterization method, including the above analysis, and its performance, discussed further, depend on specific definition of the LSP and its spectrum. Thus, it is not directly applicable to other applications, but the general approach can be easily repeated to build the characterization method anew.

3. Experimental procedures and test data

The experimental verification of the developed spectral characterization method is based on the SFC, which reliably measures LSPs of single particles for the wavelength of 660 nm in the an-

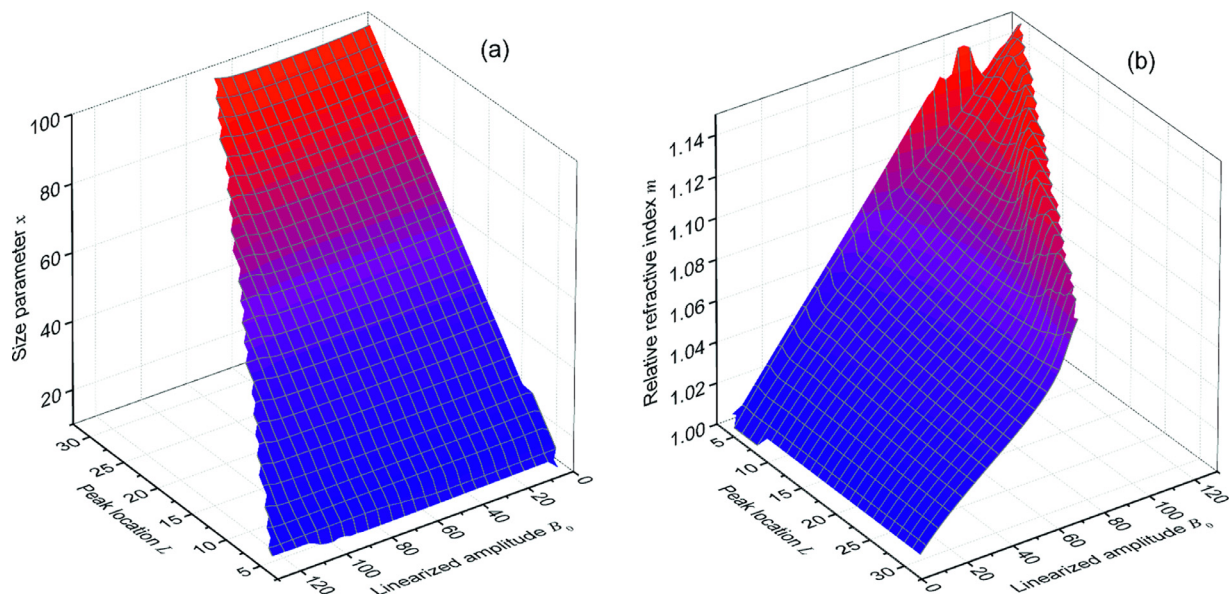


Fig. 10. Same as Fig. 9, but after the interpolation using the intermediate regular grid. Color denotes the height (the value of the z coordinate). (For interpretation of the references to color in this figure legend, the reader is referred to the web version of this article.)

gular range from 10° to 65° . Details of the SFC are described elsewhere [11,15]. We chose two relevant biological objects, which has close-to-spherical shape and (partly) fall into the uniqueness domain discussed above, namely milk fat globules and spherized red blood cells (RBCs). For both samples the absorption (imaginary part of the refractive index) at the used wavelength can be neglected.

LSP measurements for milk sample had been performed previously [49]. Briefly, whole (not normalized) milk was obtained from a local farmer. The sample was warmed to approximately 20°C prior to measurement and diluted 50,000 times with distilled water [49]. The range of sizes for those milk fat globules is $0.5\text{--}6\ \mu\text{m}$, refractive index n is $1.44\text{--}1.52$. The medium is water with $n_0 = 1.331$, leading to the range of relative refractive index m $1.08\text{--}1.14$. And the range of x is then $3\text{--}38$, which partly falls into the signal-based uniqueness domain [Fig. 7(a)].

Red blood cells were studied using the protocol described in [50]. After informed consent a blood sample was taken from a donor by venopuncture and collected in a vacuum tube containing anticoagulant. The blood was placed into lysing solution of ammonium chloride to spherize RBCs. In this case the medium refractive index is $n_0 = 1.331$. The range of x and m are [35,48] and [1.022, 1.048], respectively, which is completely inside the operational (signal-based uniqueness) domain of the method [Fig. 7(a)].

Both sets of data measured by the SFC were first processed by least-square global optimization, using the Mie theory as described in [49], and are further denoted as “LSP fit”. Thus we obtained best-fit values and uncertainties of d and n for each particle. Those were further used as a reference to evaluate the performance of the developed spectral method.

Finally, to estimate the sensitivity of the developed method to deviations from the spherical shape we used synthetic data for spheroids, as described in [51]. For that we used a database of LSPs, originally used for milk fat globules [49], and cut it to fall completely within the signal-based uniqueness domain. The resulting ranges are: volume-equivalent diameter $d_v \in [1.6, 6]\ \mu\text{m}$, aspect ratio $\varepsilon \in [1.1, 1.41]$, $n \in [1.44, 1.48]$ (with $n_0 = 1.343$), and complete range of orientation with respect to the incident beam – $[0^\circ, 90^\circ]$. Those synthetic LSPs were calculated with the T-matrix method [52].

4. Results and discussion

4.1. Milk fat globules

When turning to experimental signals corresponding uncertainties come into play. While uniform white noise has almost no influence on the LSP spectrum and, hence, on the inverse algorithm (data not shown), there are other less trivial distortions of the ideal signal of a sphere. See, for instance, a typical LSP of milk fat globule in Fig. 11(a), shown together with a best-fit theoretical LSP. The low-frequency difference between them (residual) is similar to spatial blur (running average) and has a pronounced effect on the LSP spectrum. In particular, it has almost no effect on L and A_0 , but significantly decreases A_p . It is mostly due to the deviation of the real particle shape from a spherical one, which is expected both for milk fat globules and spherized RBCs. Another factor is the instrumental distortions of the SFC, which are quantitatively similar, but are at least two times smaller in magnitude, as assessed from measurement of $4\ \mu\text{m}$ polystyrene particles assumed to be ideal spheres (data not shown). We do not analyze the latter spheres further, since they fall outside of both uniqueness domains of the characterization method. Note that in the following we show the real characteristics of the measured particles (d and n) in contrast to dimensionless ones (x and m) used in Section 2.

Also shown in Fig. 11 is the LSP calculated from the characteristics obtained from the processing of (L, A_0) . Naturally, the power spectrum of this LSP agrees with the experiment and the LSP (Mie) fit in those two parameters. However, the close agreement between the spectral method and the LSP fit as a whole, spanning from agreement of obtained characteristics [Fig. 11(a)] is somewhat surprising. Note that the simplest least-square fit is a minimization of one specific error norm, which does not exactly correspond to the complex structure of residual. Still, the two different methods give very close values, which adds confidence to application of both of them.

One can also see from Fig. 11(b) that both other spectral amplitudes (A_p and A_p/A_0) are much more sensitive to model errors. This is illustrated in Fig. A6, showing larger differences in both the

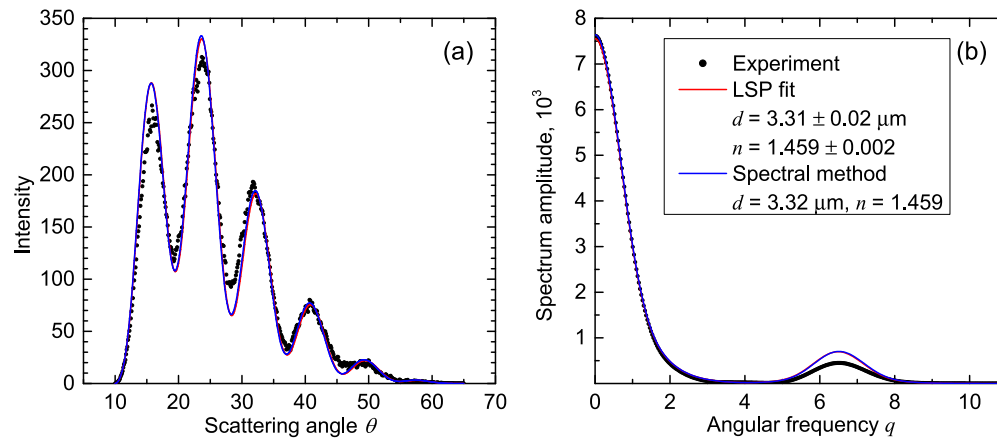


Fig. 11. Windowed LSP (a) and its power spectrum (b) for a milk fat globule, depicting experimental and two theoretical LSPs. The latter correspond to sphere characteristics obtained with least-square LSP fit and the developed inversion method based on spectral parameters (LA_0). The obtained values of characteristics are given in the legend. For the LSP fit we also show the error estimates (\pm) of this characteristics corresponding to 1 standard deviation.

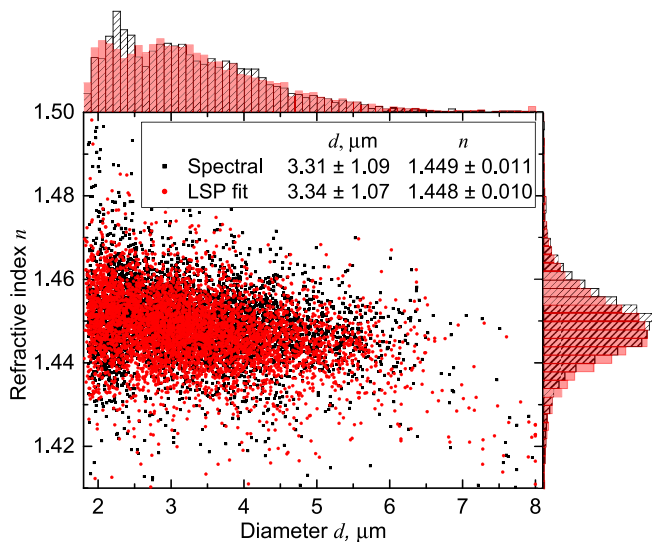


Fig. 12. Scatter plot of characterization of milk fat globules using the spectral method based on (LA_0) and the least-squares LSP fit (5181 particles). Also shown are mean and (\pm) standard deviations for particle characteristics over the whole sample. Histograms on the top and bottom sides correspond to distributions over individual characteristics; striped and red-filled bins correspond to the spectral method and the LSP fit, respectively. (For interpretation of the references to color in this figure legend, the reader is referred to the web version of this article.)

LSP and its power spectrum, resulting in systematic errors in the obtained characteristics (mostly n). Therefore, for all considered experimental targets (see also Section 4.2) the amplitude A_0 is clearly more robust with respect to distortions and leads to more accurate retrievals. That is why we treat it as the main spectral amplitude, leaving the other two for Appendix A.

Let us turn to the processing of the whole sample, shown in Fig. 12. We have employed the characterization approach based on signal-based uniqueness domain, thus part of the sample with smaller and larger sizes (about 53%) is discarded in all results. In total 5181 particles were processed. The agreement between the proposed method and the standard LSP fit is very good, both in terms of the complete distribution and its integral parameters. We also tried characterization methods, based on two other spectral amplitudes, showing the results in Fig. A7. However, the results

are definitely worse due to systematic shift in n in accordance to single-particle results discussed above. Moreover, a smaller number of particles fall into the uniqueness domains for those spectral amplitudes. Therefore, the parameters of the distributions over the whole sample (shown in the legends) cannot be compared directly.

The advantage of a more complicated LSP fit is that it additionally provides an error estimate for each characteristic, which can be considered as the best accuracy possible for a given experimental measurement. We have used those estimates for a more detailed single-particle comparison of the methods. As shown in Fig. 13, there is a correlation between the difference of two methods and the LSP-fit uncertainties. Moreover, the data is approximately symmetric with respect to the unity-slope line, suggesting that the accuracy of the spectral method is generally comparable to that of the LSP fit. Moreover, the largest deviations from the unity-slope line mostly appear for small differences, i.e. where both methods are good enough for most practical purposes. While without knowing the real characteristics of the measured particles we cannot directly assess the accuracy of the spectral method, we can claim that this error is smaller than the difference from the LSP fit plus the uncertainty of the latter. Thus, Fig. 13 shows that for many particles the spectral method is capable of accuracy better than 100 nm and 0.01 in d and n , respectively.

4.2. Spherized red blood cells

The processing of the spherized red blood cells is done completely analogous to the milk fat globules (Section 4.1). In total 4483 particles were processed, all of them satisfy the signal-based uniqueness bound. The results are shown in Figs. 14 and 15. As in the case of milk the characteristics obtained by the spectral method are very close to that of the LSP fit, and the differences between the two methods are comparable to the estimated uncertainties. However, for particles with the largest uncertainties (the least spherical shape) the differences are several times smaller than the uncertainties (Fig. 15). This does not imply that the spectral method is more accurate. Instead, it only shows that the spectral method treats shape distortions similarly to the LSP fit (see Fig. 11). Nevertheless, these results do support the conclusion that the accuracy of the spectral method is at least comparable to that of the LSP fit. The results for characterization method based on A_p are

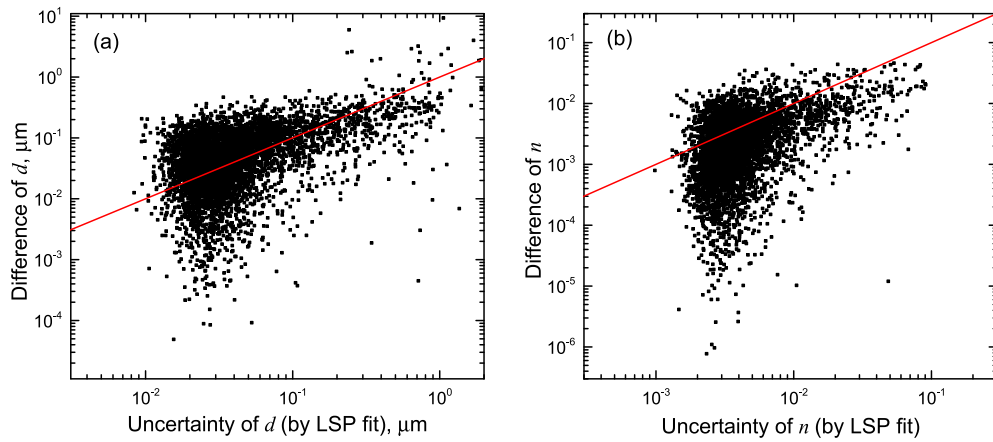


Fig. 13. Scatter plot of difference between the characteristics, d (a) or n (b), obtained by the LSP fit and the spectral method versus the uncertainty (error estimate) of the LSP fit itself in log-log scale. The straight line with the slope 1 is shown for illustration purposes. The underlying data is the same as in Fig. 12.

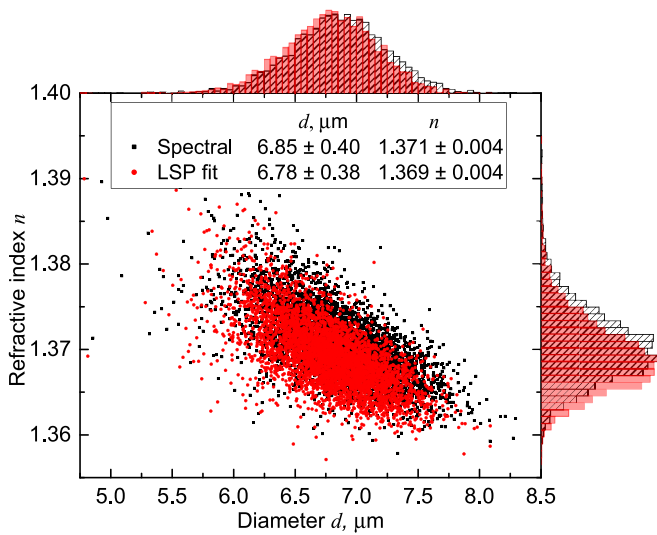


Fig. 14. Same as Fig. 12 but for the spherized red blood cells (4483 particles).

shown in Fig. A8; they are much less accurate. Using A_p/A_0 is not feasible at all for this experiment, since the distortions (systematic

decrease) of this parameter shift it outside of both uniqueness domains [Fig. A4(d)] for most of the measured particles.

4.3. Simulated spheroids

Simulated data allow us to probe the effect of shape distortions more quantitatively. We processed the 1123 synthetic LSPs and plot the resulting error of determined characteristics versus the aspect ratio ε (Fig. 16). For assessment of size values we chose (rather arbitrarily) the volume-equivalent diameter as a reference, but that does not affect the following conclusions. First, the proposed characterization method is continuous (stable) with respect to the shape distortion, i.e. the closer the particle is to a sphere – the smaller are the errors. Even for $\varepsilon = 1.4$ the obtained characteristics are qualitatively correct, although the errors of n are large. Second, we can set a convenient threshold $\varepsilon = 1.1$, below which the errors can be claimed small – mostly below 5% (relative) and 0.01 for d_v and n , respectively. The results for characterization methods, based on two other spectral amplitudes, are shown in Fig. A9. While the results of both other characterization methods are also continuous with ε , they are definitely less accurate, directly supporting the hypothesis of their larger sensitivity to shape distortions.

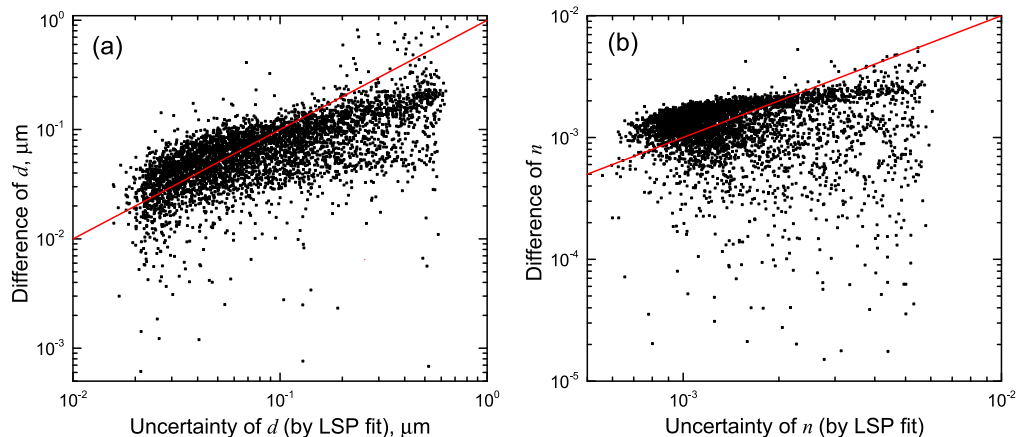


Fig. 15. Same as Fig. 13 but for the spherized red blood cells. The underlying data is the same as in Fig. 14.

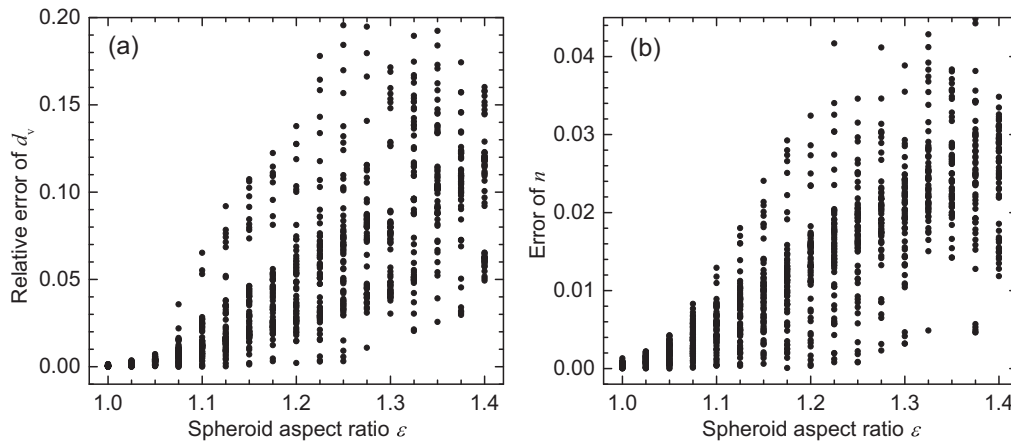


Fig. 16. Characterization of synthetic spheroids (1123 particles) with the spectral method based on (L, A_0) , showing scatter plot of relative error of d_v (a) and absolute error of n (b) versus the spheroid aspect ratio ε .

5. Conclusion

We developed a fast method to determine size and refractive index of homogeneous spheres from the power Fourier spectrum of their LSPs. To make the algorithm as simple and robust as possible we explicitly limited ourselves to using only two spectral parameters – the location of the non-zero peak (the main angular frequency) L and zero-frequency amplitude A_0 . The method is based on the interpolation of the inverse of the map from the space of the particle characteristics x and m to the space of spectral parameters L and A_0 ; hence, it works only inside the uniqueness domain of this map. Two approaches were tested for construction of this domain: based on prior assumptions about ranges of x and m , and using only the measured parameters L and A_0 . The spectral peak cannot be reliably resolved for $x < 11$, while the larger limit of x was arbitrarily set to 100. For smaller x the prior and signal-based uniqueness range of m is from 1 to 1.15 and 1.25, respectively, and for larger x the upper bound of m oscillates with decreasing trend towards 1.1.

The developed method was tested on two experimental samples, milk fat globules and spherized red blood cells, and resulted in accuracy not worse than the reference method based on the least-square fit of the LSP with the Mie theory. Moreover, for particles with significant deviation from the spherical shape the spectral method was much closer to the Mie-fit result than the estimated uncertainty of the latter. We also tested the spectral method on synthetic LSPs of spheroids with ε up to 1.4. The results are qualitatively correct for all cases; however, the good accuracy (relative errors of d_v and absolute error of n less than 5% and 0.01, respectively) was systematically obtained only for $\varepsilon < 1.1$.

The major advantage of the method is its speed – about 1 ms per LSP on a desktop computer, which is at least 3 orders of magnitude faster than the direct fit of the LSP. This allows novel applications, e.g., using it inside other iterative optimization algorithms, but comes at a cost of its limited range of applicability in terms of particle characteristics. Moreover, the method gives no indication of data quality or uncertainties of the estimated characteristics,

which can be alleviated only by considering additional parameters of either LSP or its spectrum. The robustness of the method with respect to shape and even instrumental distortions is related to the fortunate choice of A_0 as a second spectral parameter. Methods based on other two tested parameters, absolute and relative amplitudes of the non-zero spectral peak, performed fine on ideal data but led to large systematic shifts in the presence of even minor shape distortions. Hence, they were largely inferior to the method based on A_0 in all test cases.

Importantly, we not only constructed a characterization method for a specific experimental configuration, but also provided all relevant details and discussed several potential issues for its application. Therefore, it is straightforward to repeat the whole procedure for any other experimental set-up resulting in a different expression of the LSP.

Acknowledgments

Most of the work was supported by [Russian Science Foundation](#) (Grant No. 14-15-00155), while the experimental measurements of red blood cells and milk fat globules – by [Russian Foundation for Basic Research](#) (Grant numbers 16-34-00476 and 16-34-00228, respectively). D.I. Strokotov also acknowledges the support by the Stipend of the President of Russian Federation for young scientists.

Appendix A. Employing other spectral amplitudes

Here we list the results of using two other spectral amplitudes, A_p and A_p/A_0 , in combination with L for characterization of various particles. This results complement the results for (L, A_0) in the main text of the paper, and are briefly discussed there. The purpose of this Appendix is mainly to illustrate other options and the wealth of the Mie theory in general. Unfortunately, these options are much more sensitive to the particle shape distortions (see, e.g., [Figs. A6 and A9](#)), making them clearly inferior to characterization based on (L, A_0) in most experimental settings.

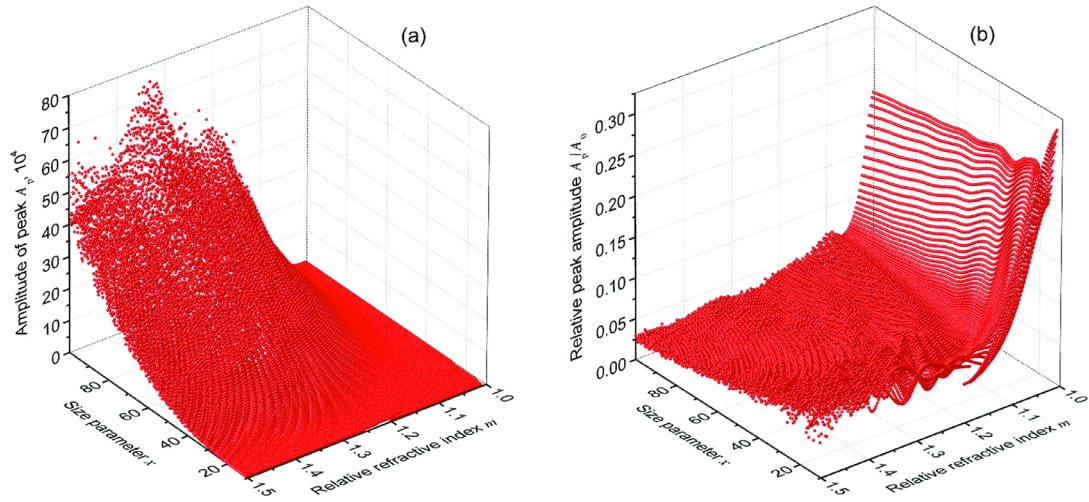


Fig. A1. Same as Fig. 4(b), but for A_p (a) and A_p/A_0 (b).

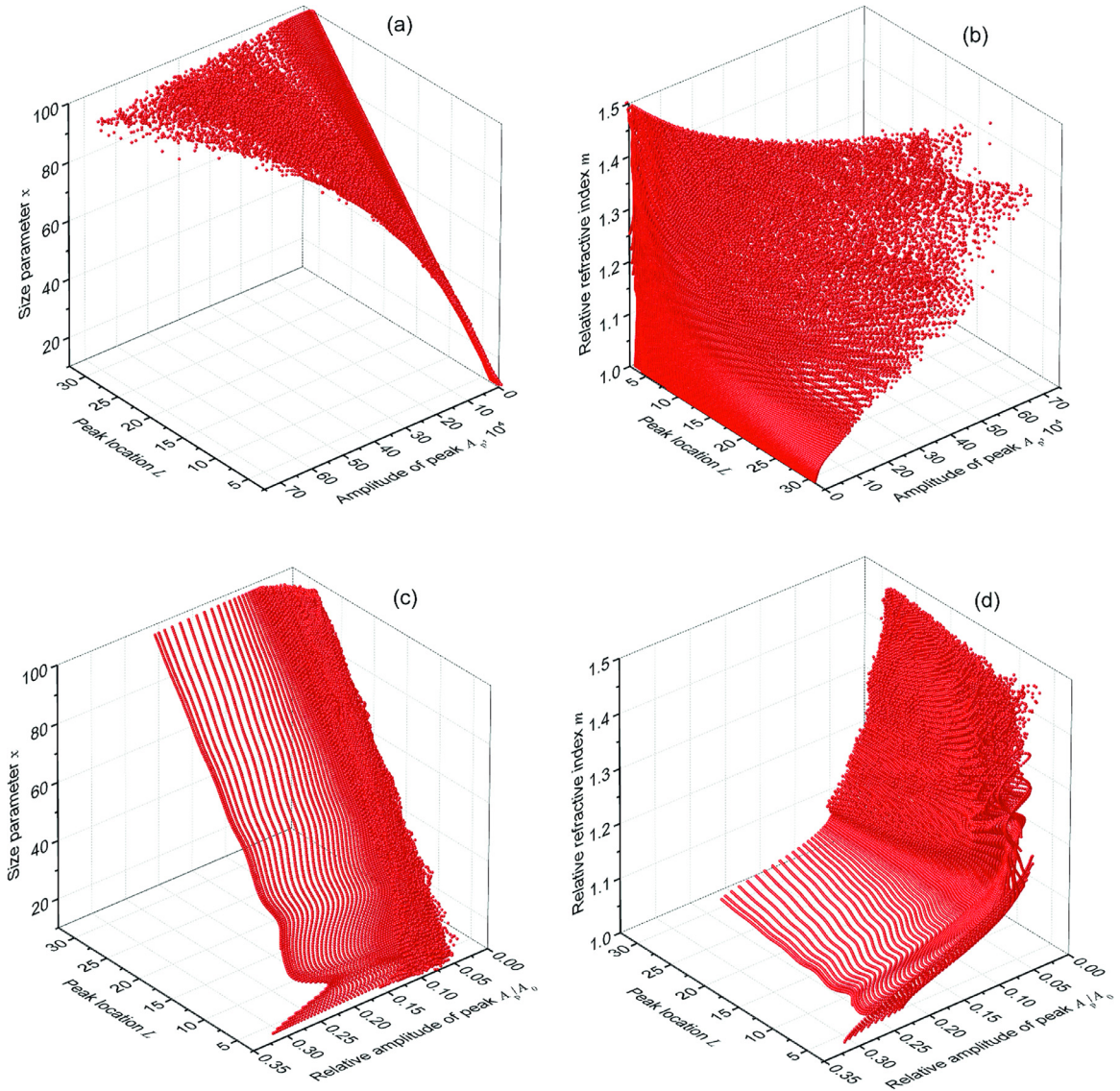


Fig. A2. Same as Fig. 5, but using A_p (a,b) and A_p/A_0 (c,d) as a second spectral parameter. It is based on the same data as Fig. 4(a) and Fig. A1. Axes directions vary among the figure parts for clarity.

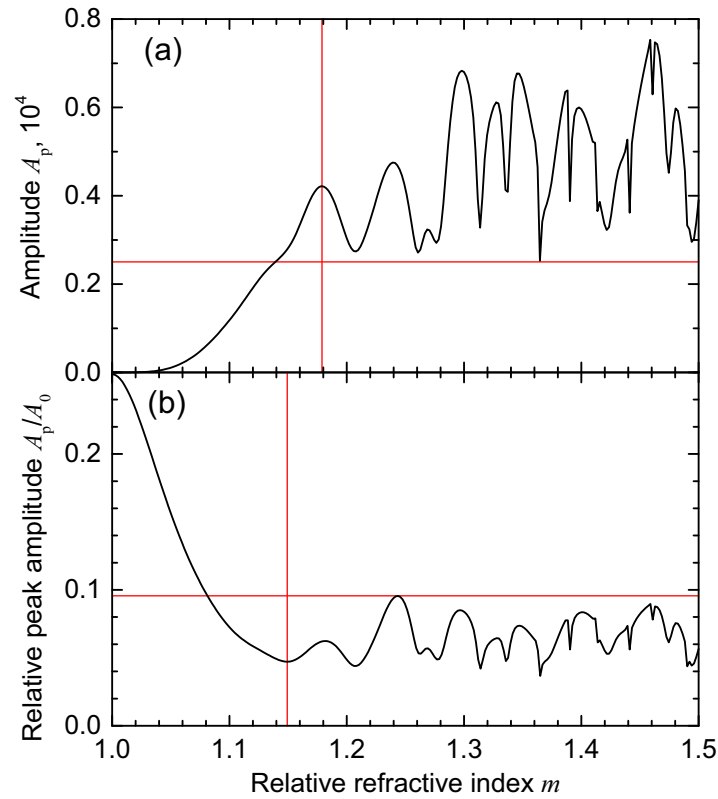


Fig. A3. Same as Fig. 6, but for A_p (a) and A_p/A_0 (b). Note that the latter is a decreasing function of m inside its uniqueness domain. Red lines denote thresholds for m and amplitude, used to define corresponding uniqueness domains. (For interpretation of the references to color in this figure legend, the reader is referred to the web version of this article.)

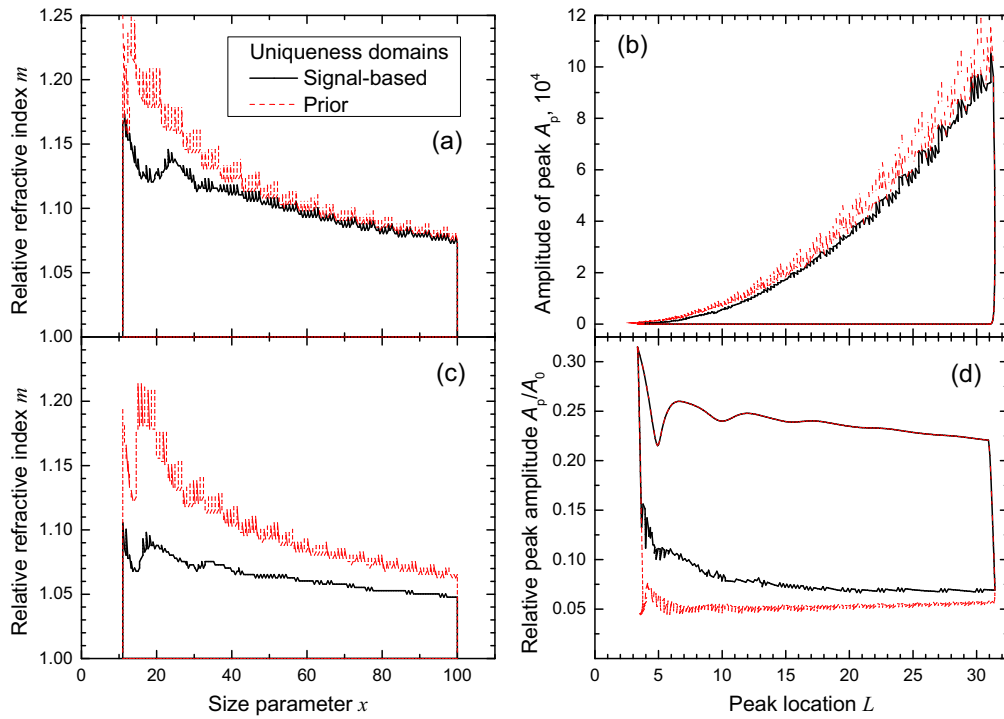


Fig. A4. Same as Fig. 7, but using A_p (a,b) and A_p/A_0 (c,d) as a second spectral parameter. In part (d) top boundaries for both uniqueness domains coincide, analogously to the bottom boundaries in other parts and Fig. 7.

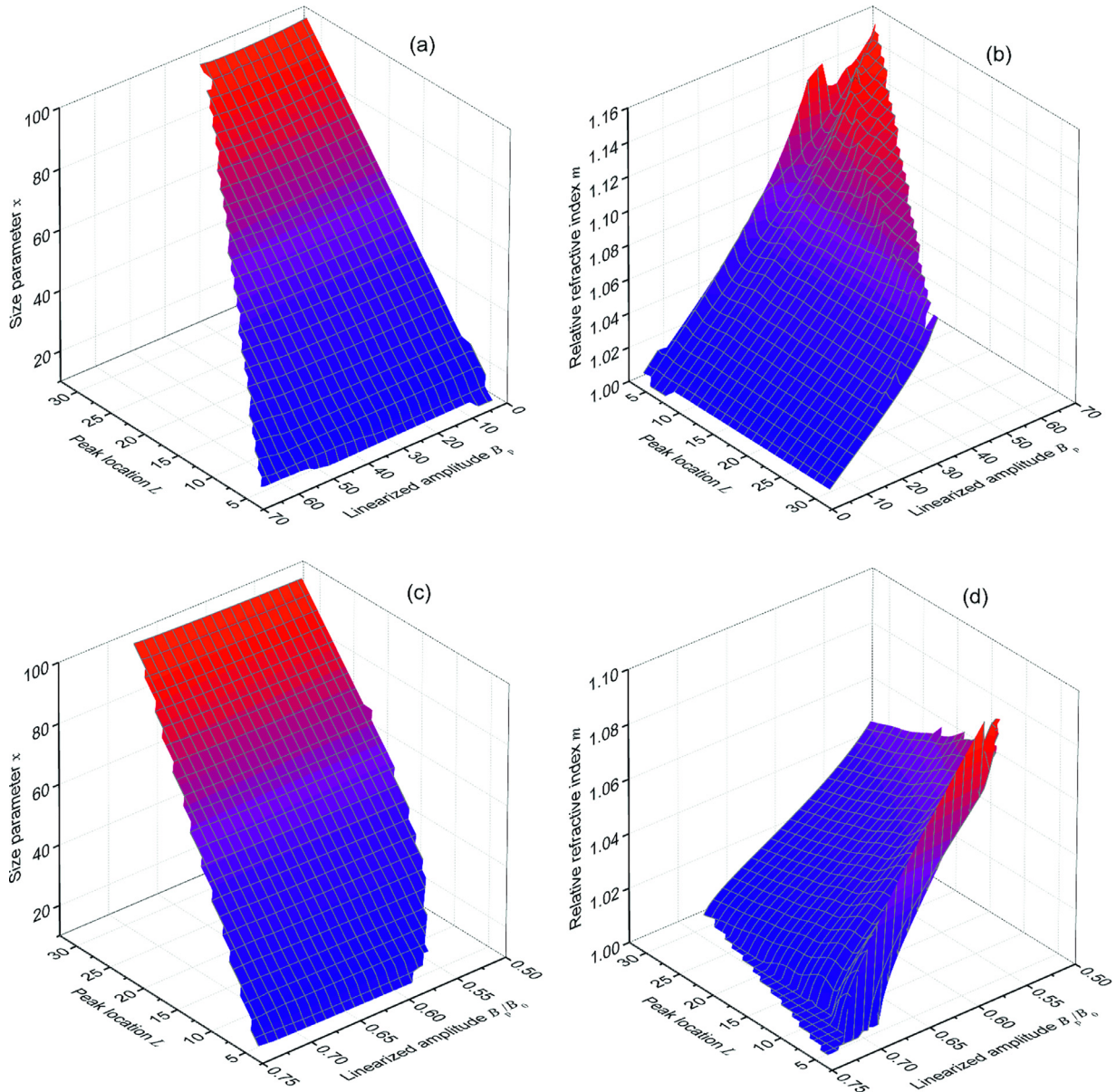


Fig. A5. Same as Fig. 10, but using B_p (a,b) and B_p/B_0 (c,d) as a second spectral parameter. The operational domains correspond to the signal-based uniqueness domains, depicted in Fig. A4.

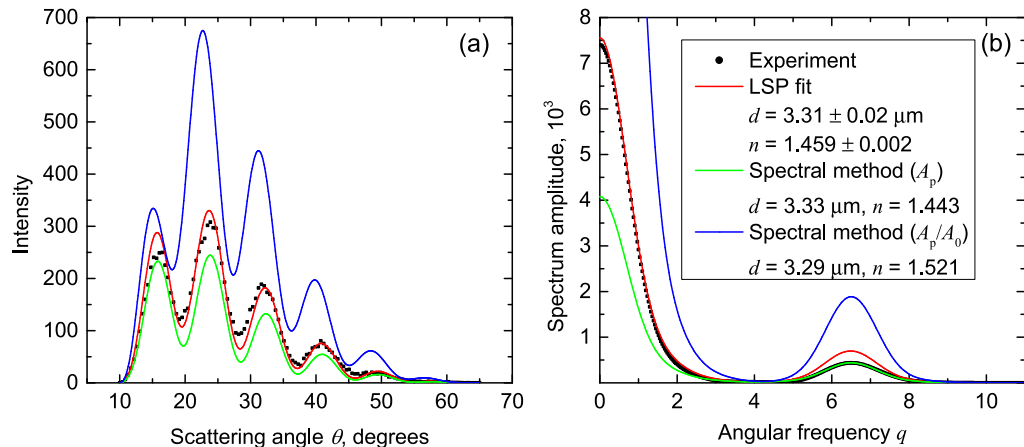


Fig. A6. Same as Fig. 11 but using A_p and A_p/A_0 as a second spectral parameter.

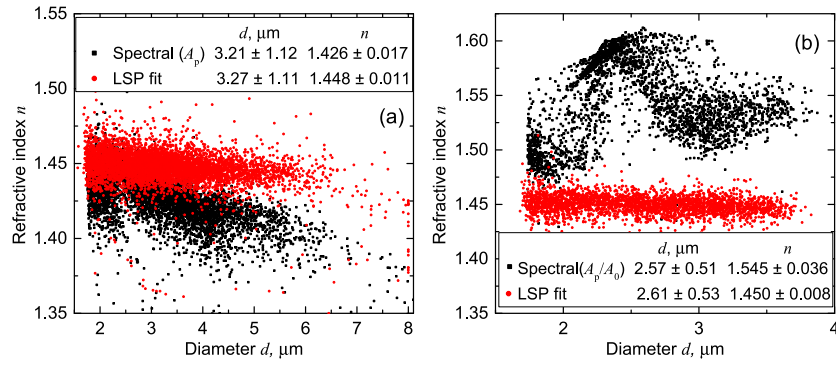


Fig. A7. Same as Fig. 12 but without histograms and using A_p (a) and A_p/A_0 (b) as a second spectral parameter. We employed the prior uniqueness domain in (b), since almost all data fall outside of the signal-based one [Fig. A4(d)] due to the reduced values of A_p/A_0 in the experiment. The number of processed particles, i.e. falling into the corresponding uniqueness domains, is 5485 and 2897 for (a) and (b), respectively.

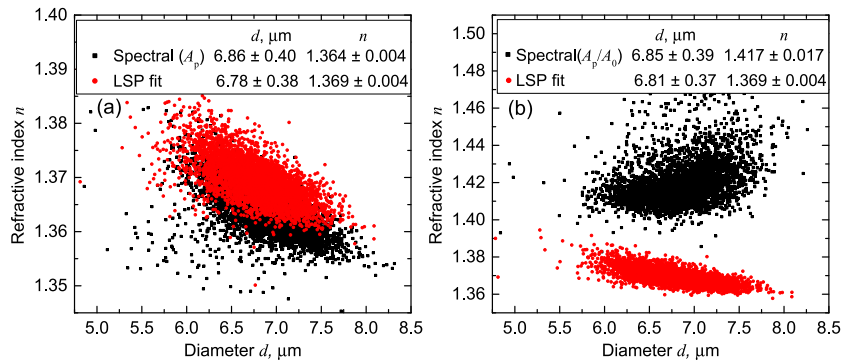


Fig. A8. Same as Fig. 14 but using A_p (a) and A_p/A_0 (b) as a second spectral parameter. Analogously to Fig. A7(b) we employed the prior uniqueness domain in part (b). The number of processed particles, i.e. falling into the corresponding uniqueness domains, is 4483 and 4271 for (a) and (b), respectively.

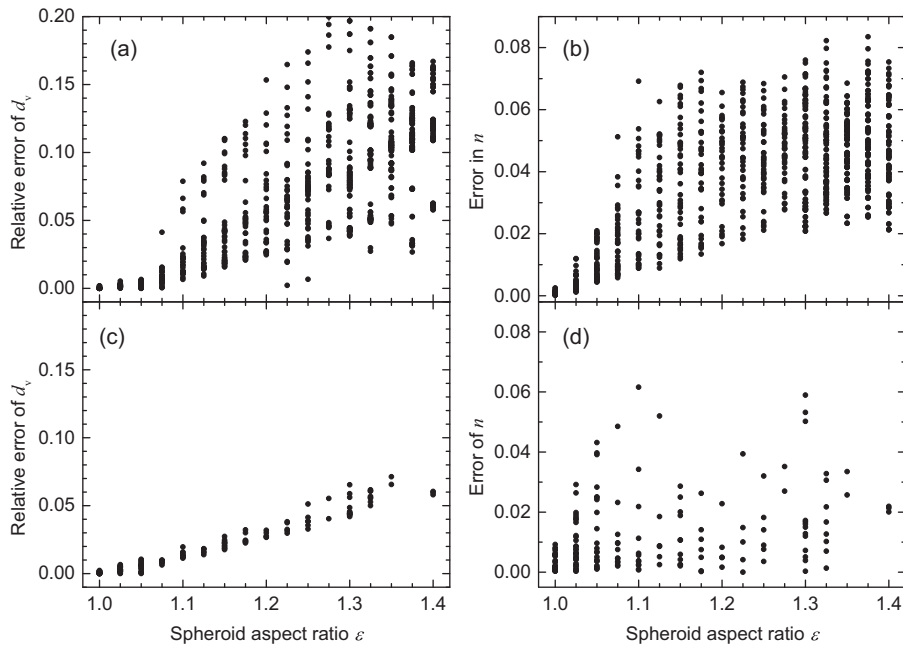


Fig. A9. Same as Fig. 16 but using A_p (a,b) and A_p/A_0 (c,d) as a second spectral parameter. Analogously to Fig. A7(b) we employed the prior uniqueness domain in parts (c,d). The number of processed particles, i.e. falling into the corresponding uniqueness domains, is 961 and 197 for (a,b) and (c,d), respectively.

References

- [1] Mishchenko MI, Hovenier JW, Travis LD, editors. Light scattering by nonspherical particles, theory, measurements, and applications. New York: Academic Press; 2000.
- [2] Doicu A, Trautmann T, Schreier F. Numerical regularization for atmospheric inverse problems. Heidelberg: Springer; 2010.
- [3] Hassan PA, Rana S, Verma G. Making sense of Brownian motion: colloid characterization by dynamic light scattering. *Langmuir* 2015;31:3–12.
- [4] Mishchenko MI, Dlugach JM, Yurkin MA, Bi L, Cairns B, Liu L, et al. First-principles modeling of electromagnetic scattering by discrete and discretely heterogeneous random media. *Phys Rep* 2016;632:1–75.
- [5] Anderson W, Kozak D, Coleman VA, ÅK Jämting, Trau M. A comparative study of submicron particle sizing platforms: accuracy, precision and resolution analysis of polydisperse particle size distributions. *J Colloid Interface Sci* 2013;405:322–30.
- [6] Maltsev VP, Semyanov KA. Characterisation of bio-particles from light scattering. Utrecht: VSP; 2004.
- [7] Kinnunen M, Karmenyan A. Overview of single-cell elastic light scattering techniques. *J Biomed Opt* 2015;20:051040.
- [8] Tycko DH, Metz MH, Epstein EA, Grinbaum A. Flow-cytometric light scattering measurement of red blood cell volume and hemoglobin concentration. *Appl Opt* 1985;24:1355–65.
- [9] Konokhova AI, Chernova DN, Strokotov DI, Karpenko AA, Chernyshev AV, Maltsev VP, et al. Light-scattering gating and characterization of plasma microparticles. *J Biomed Opt* 2016;21:115003.
- [10] Ludlow IK, Kaye PH. A scanning diffractometer for the rapid analysis of microparticles and biological cells. *J Colloid Interface Sci* 1979;69:571–89.
- [11] Maltsev VP. Scanning flow cytometry for individual particle analysis. *Rev Sci Instrum* 2000;71:243–55.
- [12] Kaye PH. Spatial light-scattering analysis as a means of characterizing and classifying non-spherical particles. *Meas Sci Technol* 1998;9:141.
- [13] Giacomelli M, Zhu Y, Lee J, Wax A. Size and shape determination of spheroidal scatterers using two-dimensional angle resolved scattering. *Opt Express* 2010;18:14616–26.
- [14] Wriedt T. Light scattering theory and programs: discussion of latest advances and open problems. *J Quant Spectrosc Radiat Transf* 2012;113:2465–9.
- [15] Strokotov DI, Moskalensky AE, Nekrasov VM, Maltsev VP. Polarized light-scattering profile - advanced characterization of nonspherical particles with scanning flow cytometry. *Cytometry A* 2011;79A:570–9.
- [16] Gilev KV, Yurkin MA, Chernyshova ES, Strokotov DI, Chernyshev AV, Maltsev VP. Mature red blood cells: from optical model to inverse light-scattering problem. *Biomed Opt Express* 2016;7:1305–10.
- [17] Kim Y, Shim H, Kim K, Park H, Jang S, Park Y. Profiling individual human red blood cells using common-path diffraction optical tomography. *Sci Rep* 2014;4:6659.
- [18] Hosseinizadeh A, Dashti A, Schwander P, Fung R, Ourmazd A. Single-particle structure determination by X-ray free-electron lasers: possibilities and challenges. *Struct Dyn* 2015;2:041601.
- [19] Mudry E, Chaumet PC, Belkebir K, Sentenac A. Electromagnetic wave imaging of three-dimensional targets using a hybrid iterative inversion method. *Inverse Probl* 2012;28:065007.
- [20] Colton D, Kress R. Inverse acoustic and electromagnetic scattering theory, 93. 3rd ed. New York: Springer; 2013.
- [21] Wang A, Garmann RF, Manoharan VN. Tracking E. coli runs and tumbles with scattering solutions and digital holographic microscopy. *Opt Express* 2016;24:23719–25.
- [22] Kolesnikova IV, Potapov SV, Yurkin MA, Hoekstra AG, Maltsev VP, Semyanov KA. Determination of volume, shape and refractive index of individual blood platelets. *J Quant Spectrosc Radiat Transf* 2006;102:37–45.
- [23] Pyhtila JW, Wax A. Polarization effects on scatterer sizing accuracy analyzed with frequency-domain angle-resolved low-coherence interferometry. *Appl Opt* 2007;46:1735–41.
- [24] Wojtkiewicz S, Sawosz P, Kostecki M, Sokolowska A. Optical method for characterization of nanoplates in lyosol. *Microelectron Eng* 2013;108:121–6.
- [25] Caramanica F. A method based on particle swarm optimization to retrieve the shape of red blood cells: a preliminary assessment. *Prog Electromagn Res M* 2012;27:109–17.
- [26] Moskalensky AE, Yurkin MA, Konokhova AI, Strokotov DI, Nekrasov VM, Chernyshev AV, et al. Accurate measurement of volume and shape of resting and activated blood platelets from light scattering. *J Biomed Opt* 2013;18:017001.
- [27] Konokhova AI, Gelash AA, Yurkin MA, Chernyshev AV, Maltsev VP. High-precision characterization of individual E. coli cell morphology by scanning flow cytometry. *Cytometry A* 2013;83:568–75.
- [28] Strokotov DI, Yurkin MA, Gilev KV, van Bockstaele DR, Hoekstra AG, Rubtsov NB, et al. Is there a difference between T- and B-lymphocyte morphology. *J Biomed Opt* 2009;14:064036.
- [29] Haykin S. Neural Networks: a comprehensive foundation. 2nd ed. Englewood Cliffs, NJ: Prentice Hall; 1998.
- [30] Ulanowski Z, Wang Z, Kaye PH, Ludlow IK. Application of neural networks to the inverse light scattering problem for spheres. *Appl Opt* 1998;37:4027–33.
- [31] Berdnik VV, Gilev K, Shvalov A, Maltsev V, Loiko VA. Characterization of spherical particles using high-order neural networks and scanning flow cytometry. *J Quant Spectrosc Radiat Transf* 2006;102:62–72.
- [32] Apostolopoulos G, Tsinoopoulos SV, Dermatas E. A methodology for estimating the shape of biconcave red blood cells using multicolor scattering images. *Biomed Signal Process Control* 2013;8:263–72.
- [33] Berdnik VV, Loiko VA. Neural networks for particle parameter retrieval by multi-angle light scattering. In: Light scattering reviews 10. Heidelberg: Springer; 2016. p. 291–340.
- [34] Quist GM, Wyatt PJ. Empirical solution to the inverse-scattering problem by the optical strip-map technique. *J Opt Soc Am A* 1985;2:1979–85.
- [35] Maltsev VP, Lopatin VN. Parametric solution of the inverse light-scattering problem for individual spherical particles. *Appl Opt* 1997;36:6102–8.
- [36] Zhang L, Chen X, Zhang Z, Chen W, Zhao H, Zhao X, et al. Scattering pulse of label free fine structure cells to determine the size scale of scattering structures. *Rev Sci Instrum* 2016;87:044301.
- [37] Min SL, Gomez A. High-resolution size measurement of single spherical particles with a fast Fourier transform of the angular scattering intensity. *Appl Opt* 1996;35:4919–26.
- [38] Yu S, Zhang J, Moran MS, Lu JQ, Feng Y, Hu X-H. A novel method of diffraction imaging flow cytometry for sizing microspheres. *Opt Express* 2012;20:22245–51.
- [39] Ludlow IK, Everitt J. Application of Gegenbauer analysis to light-scattering from spheres - theory. *Phys Rev E* 1995;51:2516–26.
- [40] Steiner B, Berge B, Gausmann R, Rohmann J, Rühl E. Fast in situ sizing technique for single levitated liquid aerosols. *Appl Opt* 1999;38:1523–9.
- [41] Jacobs KM, Lu JQ, Hu X-H. Development of a diffraction imaging flow cytometer. *Opt Lett* 2009;34:2985–7.
- [42] Jakubczyk D, Derkachov G, Kolwas M, Kolwas K. Combining weighting and scatterometry: application to a levitated droplet of suspension. *J Quant Spectrosc Radiat Transf* 2013;126:99–104.
- [43] Semyanov KA, Tarasov PA, Zharinov AE, Chernyshev AV, Hoekstra AG, Maltsev VP. Single-particle sizing from light scattering by spectral decomposition. *Appl Opt* 2004;43:5110–15.
- [44] Semyanov KA, Zharinov AE, Tarasov PA, Yurkin MA, Skribunov IG, van Bockstaele DR, et al. Optics of leucocytes. In: Hoekstra AG, Maltsev VP, Videen G, editors. Optics of biological particles. Dordrecht: Springer; 2007. p. 269–80.
- [45] Tarasov PA, Yurkin MA, Avrorov PA, Semyanov KA, Hoekstra AG, Maltsev VP. Optics of erythrocytes. In: Hoekstra AG, Maltsev VP, Videen G, editors. Optics of biological particles. Dordrecht: Springer; 2007. p. 243–59.
- [46] Fiorani L, Maltsev VP, Nekrasov VM, Palucci A, Semyanov KA, Spizzichino V. Scanning flow cytometer modified to distinguish phytoplankton cells from their effective size, effective refractive index, depolarization, and fluorescence. *Appl Opt* 2008;47:4405–12.
- [47] Bohren CF, Huffman DR. Absorption and scattering of light by small particles. New York: Wiley; 1983.
- [48] Yurkin MA. Discrete dipole simulations of light scattering by blood cells PhD thesis. Amsterdam: University of Amsterdam; 2007.
- [49] Konokhova AI, Rodionov AA, Gilev KV, Mikhaelis IM, Strokotov DI, Moskalensky AE, et al. Enhanced characterisation of milk fat globules by their size, shape and refractive index with scanning flow cytometry. *Int Dairy J* 2014;39:316–23.
- [50] Chernyshova ES, Zaikina YS, Tsvetovskaya GA, Strokotov DI, Yurkin MA, Serebrennikova ES, et al. Influence of magnesium sulfate on HCO₃/Cl transmembrane exchange rate in human erythrocytes. *J Theor Biol* 2016;393:194–202.
- [51] Gilev KV, Yurkin MA, Dyatlov GV, Chernyshev AV, Maltsev VP. An optimization method for solving the inverse Mie problem based on adaptive algorithm for construction of interpolating database. *J Quant Spectrosc Radiat Transf* 2013;131:202–14.
- [52] Mishchenko MI, Travis LD. Capabilities and limitations of a current FORTRAN implementation of the T-matrix method for randomly oriented, rotationally symmetric scatterers. *J Quant Spectrosc Radiat Transf* 1998;60:309–24.